communications physics

Article

https://doi.org/10.1038/s42005-024-01776-6

Visualizing plasmons and ultrafast kinetic instabilities in laser-driven solids using X-ray scattering

Paweł Ordyna[1,2] ✉, Carsten Bähtz[1], Erik Brambrink[3], Michael Bussmann[1], Alejandro Laso Garcia[1], Marco Garten[1,6], Lennart Gaus[1,2], Sebastian Göde[3], Jörg Grenzer[1], Christian Gutt[4], Hauke Höppner[1], Lingen Huang[1], Uwe Hübner[5], Oliver Humphries[3], Brian Edward Marré[1,2], Josefine Metzkes-Ng[1], Thomas Miethlinger[1,2], Motoaki Nakatsutsumi[3], Özgül Öztürk[4], Xiayun Pan[1,2], Franziska Paschke-Brühl[1], Alexander Pelka[1], Irene Prencipe[1], Thomas R. Preston[3], Lisa Randolph[3,4], Hans-Peter Schlenvoigt[1], Jan-Patrick Schwinkendorf[1,3], Michal Šmíd[1], Sebastian Starke[1], Radka Štefaníková[1,2], Erik Thiessenhusen[1,2], Toma Toncian[1], Karl Zeil[1], Ulrich Schramm[1,2], Thomas E. Cowan[1,2] & Thomas Kluge[1] ✉

Ultra-intense lasers that ionize atoms and accelerate electrons in solids to near the speed of light can lead to kinetic instabilities that alter the laser absorption and subsequent electron transport, isochoric heating, and ion acceleration. These instabilities can be difficult to characterize, but X-ray scattering at keV photon energies allows for their visualization with femtosecond temporal resolution on the few nanometer mesoscale. Here, we perform such experiment on laser-driven flat silicon membranes that shows the development of structure with a dominant scale of 60 nm in the plane of the laser axis and laser polarization, and 95 nm in the vertical direction with a growth rate faster than 0.1 fs^{-1}. Combining the XFEL experiments with simulations provides a complete picture of the structural evolution of ultra-fast laser-induced plasma density development, indicating the excitation of plasmons and a filamentation instability. Particle-in-cell simulations confirm that these signals are due to an oblique two-stream filamentation instability. These findings provide new insight into ultra-fast instability and heating processes in solids under extreme conditions at the nanometer level with possible implications for laser particle acceleration, inertial confinement fusion, and laboratory astrophysics.

Visualizing, understanding, and controlling laser absorption, isochoric heating, particle acceleration, and other relativistic non-linear physics that occur at the interaction of powerful lasers with solids is important for applications ranging from next-generation laser ion accelerators (LIA) for medical use[1] to high-energy density physics including laboratory astrophysics[2] and inertial confinement fusion[3,4]. Only recently, (proton) fast ignition for inertial confinement fusion has gained renewed interest as a viable path towards commercialization of Inertial Fusion Energy[5–7] after the breakthrough fusion ignition achievements at the National Ignition Facility (NIF)[8,9].

Of special relevance is the understanding and control of plasma instabilities that can occur on largely different spatial, temporal, and plasma density scales. For example, compression and ignition of fusion targets in indirect-drive experiments carried out e.g. at the NIF nanosecond laser rely on the conversion of the laser energy into a homogeneous radiation field by laser-self-generated grating structures at the hohlraum entrance[10], and stabilizing instability growth that happens on the scale of 10s of microns during the capsule compression[11]. Small fluctuations in the radiation pressure on the pellet surface or in the particle heater pulse would otherwise drive instabilities there, inhibiting maximum compression or heating[12,13]. Here we focus on ultrafast relativistic instabilities that grow over a few or tens of femtoseconds that are important e.g. in fusion fast ignition scenarios (FIS)[14–16] that could potentially allow for a much better efficiency. A high-intensity short pulse laser generates a dense particle beam that heats the

[1]Helmholtz-Zentrum Dresden-Rossendorf, Dresden, Germany. [2]Technical University Dresden, Dresden, Germany. [3]European XFEL, Schenefeld, Germany. [4]Universität Siegen, Siegen, Germany. [5]Leibniz Institute of Photonic Technology, Jena, Germany. [6]Present address: Lawrence Berkeley National Laboratory, Berkeley, CA, USA. ✉e-mail: p.ordyna@hzdr.de; t.kluge@hzdr.de

high-density core and ignites the thermonuclear reaction. On their path, the relativistic electrons are susceptible to beam-plasma instabilities that occur typically on scales of the skin depth, i.e. 10s of nanometers. On the path from laser particle acceleration to application as an ignitor such instabilities are amongst the long-standing crucial physics processes that need to be understood in simulations or experimental test-beds[17]. Theories for instabilities in relativistic high-intensity laser interaction with solids fall into two categories: (i) hydrodynamic instabilities growing at interfaces between two fluid-like plasma or photon ensembles, or (ii) kinetic instabilities that occur e.g. when one plasma streams through the other. Whether one or the other dominates depends on the detailed laser and solid properties. For example, in solids with a structured surface, or driven by lasers with a shallow rising edge, laser absorption to relativistic electron currents reaches up to nearly 100%, emphasizing the kinetic streaming instabilities at the front surface[18,19] or at the rear of the target[20–22], e.g. two-stream instability (TSI), Weibel instability (WI), or current filamentation instability (CFI). On the other hand, strong hydrodynamic Rayleigh-Taylor-like instabilities (RTI) following two-plasmon decay or parametric instabilities at the front of plasmas can be dominant for materials consisting of light ions, or driven by ultra-short high-contrast laser pulses, and can break up the laser to electron coupling and inhibit streaming instabilities[23–29].

The physics of these fast few femtosecond, few nanometer plasma instability dynamics and merging to the micron-scale after a few picoseconds in high-intensity laser-driven solids is one of the large unsolved issues in high-intensity laser plasma science, but its direct observation has previously not been possible because of the small time and few nanometer length scales involved. Microscopic interpretations were therefore primarily based on simulations[24,26,27,30–33] and indirect measurements, e.g. via optical microscopy[34], interferometry[35,36], spectroscopy[37], Faraday rotation[38], or radiography[20,21,39] or the impact on the divergence of the electron beam[40]. Here, we demonstrate experimentally that such instabilities indeed exist also in the hot solid density plasmas, quantify the strength, and give limits to the growth rate.

Recent advances in the time-resolved diffraction, based on ultra-fast X-ray pulses from X-ray free-electron lasers (XFELs), now enable us to investigate laser-produced plasmas with nanometer spatial and femtosecond temporal resolution[41–46]. The novelty of the present work is not the technique (which is indeed very similar to the setup used in refs. 43,46) nor the specific physical scenario probed with the technique. In fact, since the scenario is of high relevance for FIS or LIA, there exists an exhaustive theoretical work (e.g. refs. 18,47–53). The novelty of the work is rather that it is a direct observation of laser-induced instabilities in ultra-intense laser-solid interaction with few tens of nanometer and femtosecond spatial and temporal resolution. Most of the previous studies using XFELs to reveal the structure in ultra-high intensity (UHI) laser-solid interaction focused on the irradiation and ablation of gratings or other pre-structured targets. Other studies that investigated current and two-stream instabilities were limited to the regime of lower plasma densities and/or sub-relativistic laser intensities, and did not provide the temporal and spatial resolution required for high plasma density[20,21,38,54–56]. Here, we open a new window for observations of structural dynamics induced by the laser interaction with solids, not relying on prefabricated structures anymore, which allows for benchmarking of the laser absorption, laser generated electron currents, as well as thermalization, and diffusion processes. Specifically, by variation of the laser and target parameters one can map out the instability spectrum of the fastest growing mode, i.e. the growth rate as a function of the instability wave vector, and get access to the dielectric tensor. This, in turn, is determined by the particle momentum distribution function, which, together with its temporal evolution, could thus be measured in pump-probe Small-angle X-ray scattering (SAXS) experiments.

Here, we demonstrate the feasibility of this approach by showing the experimental realization of probing the predicted nanoscopic instability growth over few femtoseconds. This proved difficult in the past, as the world's most powerful optical drive lasers need to be combined with the most advanced X-ray sources, and experiments faced fundamental challenges such as the parasitic bremsstrahlung generation and self emission of the warm or hot dense plasma that can outshine the signal.

A tightly connected phenomenon that occurs when laser-accelerated electron beams propagate through dense plasmas is the generation of bulk plasmons (BP). For example, BPs in solids can anomalously heat the bulk[57] or decay into surface plasmons[26] that due to their unique properties are a building block with several applications[58], e.g. accelerating electrons and ions[59], generating XUV radiation, and isocorically heating the surface.

With the recent completion[60] and commissioning of the Helmholtz International Beamline for Extreme Fields (HIBEF[61]) at the European XFEL[62,63], the quest for visualising few-femtosecond, few-nanometer scale non-linear plasma dynamics in ultra-short pulse UHI laser interaction with solids has begun. One primary goal of HIBEF, as well as this work, is to provide experimental benchmarks for high energy density science, including the measurement and characterization of kinetic instabilities in order to validate codes and theoretical models, and to optimize laser absorption and successive processes for above-mentioned applications. HIBEF combines a short-pulse Titanium:Sapphire UHI laser (ReLaX[60]) with the European XFEL beam. The ReLaX laser reaches its highest intensity of $5 \cdot 10^{20}\,\mathrm{Wcm}^{-2}$ when it is focused down to a 4.7 μm full width at half maximum (FWHM) focal spot and compressed to $\tau_L = 30$ fs pulse duration, exceeding the laser intensity at other XFELs by approx. an order of magnitude[60]. One enabling technology that was developed by our group for HIBEF is a SAXS detection system designed primarily to suppress radiation background. Parasitic radiation is not only suppressed by carefully designed lead shielding inside the chamber, at the chamber exit window, and around the X-ray camera. Crucially, we developed a passive radiation background suppression system, i.e. a set of HAPG (Highly Annealed Pyrolitic Graphite) X-ray crystals[64] between the solid target and the SAXS detector. They act as a chromatic X-ray mirror that separates the signal 8 keV X-ray energy from the background. We thereby effectively suppressed almost any X-ray background and plasma self-emission, which at ultra-relativistic laser intensities above $10^{20}\,\mathrm{Wcm}^{-2}$ would otherwise outshine the signal. Additionally, it is quite likely that in earlier studies employing sub-relativistic laser intensity the structure development was not sufficiently strong to be detected.

To the best of our knowledge, this is the first study combining a UHI laser, flat solid targets and an XFEL probe, enabling us to measure the signal generated by relativistic instabilities driven by a UHI short-pulse laser. We combine those measurements with particle-in-cell (PIC) simulations and further numerical analysis to understand the complex plasma dynamics in the experiment.

Results

We measured time-resolved SAXS patterns with sufficient momentum transfer range that provides, with the current setup (Fig. 1), sensitivity for correlation structures up to ≅100 nm. Larger correlations are not accessible due to a gap in the HAPG mirror that lets the unscattered XFEL beam toward a beam dump. Since the detector covers only the small angle q-range, the signal is essentially given by the time integration of the Fourier transform absolute square of the time retarded electron density integrated along the XFEL beam direction

$$I(\mathbf{q}) \propto \int_t |\mathcal{F}_{\mathbf{r}}(E_X(\mathbf{r},t)\tilde{n}_e(\mathbf{r},t))|^2 \mathrm{d}t, \tag{1}$$

where $\tilde{n}_e(\mathbf{r},t) = \int_z n_e(x,y,z,t' = t + z/c)\mathrm{d}z$ is the time retarded electron density projection and E_X is the XFEL electric field amplitude.

Figure 2 shows the measured scattering patterns as a function of probe delay from probing flat 2 μm thin silicon (Si) membranes irradiated by the ReLaX UHI laser at maximum intensity under 45° angle of incidence and p-polarization. Each main shot was accompanied by a pre-shot and a post-shot XFEL-only pulse train on the same spot (for the pre-shots the XFEL transmission was reduced by a factor of 6×10^{-4}, in order to protect the target from X-ray damage). This enabled us to verify the cold membrane quality, and to subtract parasitic signal in the background. The scattering

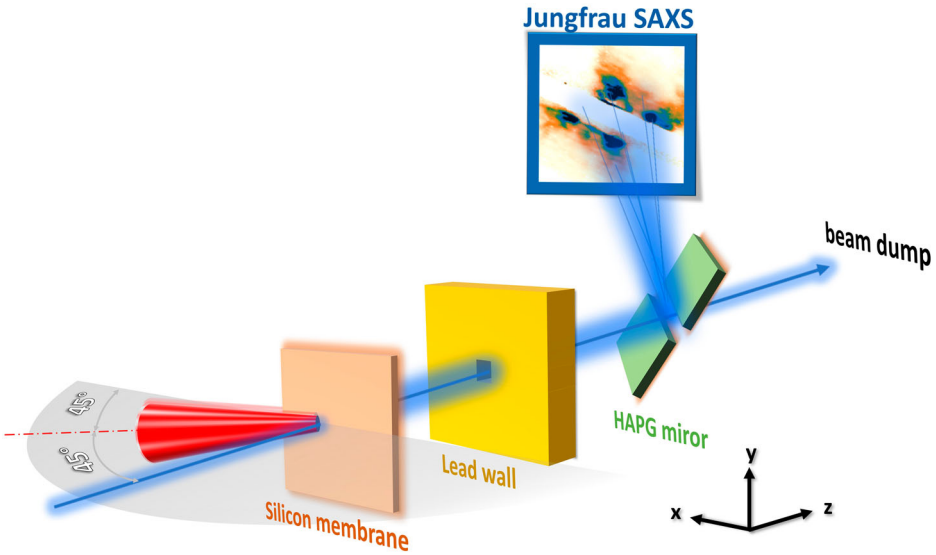

Fig. 1 | Experimental setup. The ReLaX UHI laser (red) is focused onto the Silicon membrane target under 45° in p-polarization, the XFEL (blue) is probing the plasma density under target normal direction. The Jungfrau CCD detector records the Small-angle X-ray scattering (SAXS) image reflected from the Highly Annealed Pyrolitic Graphite (HAPG) chromatic mirror. The figure is not to scale.

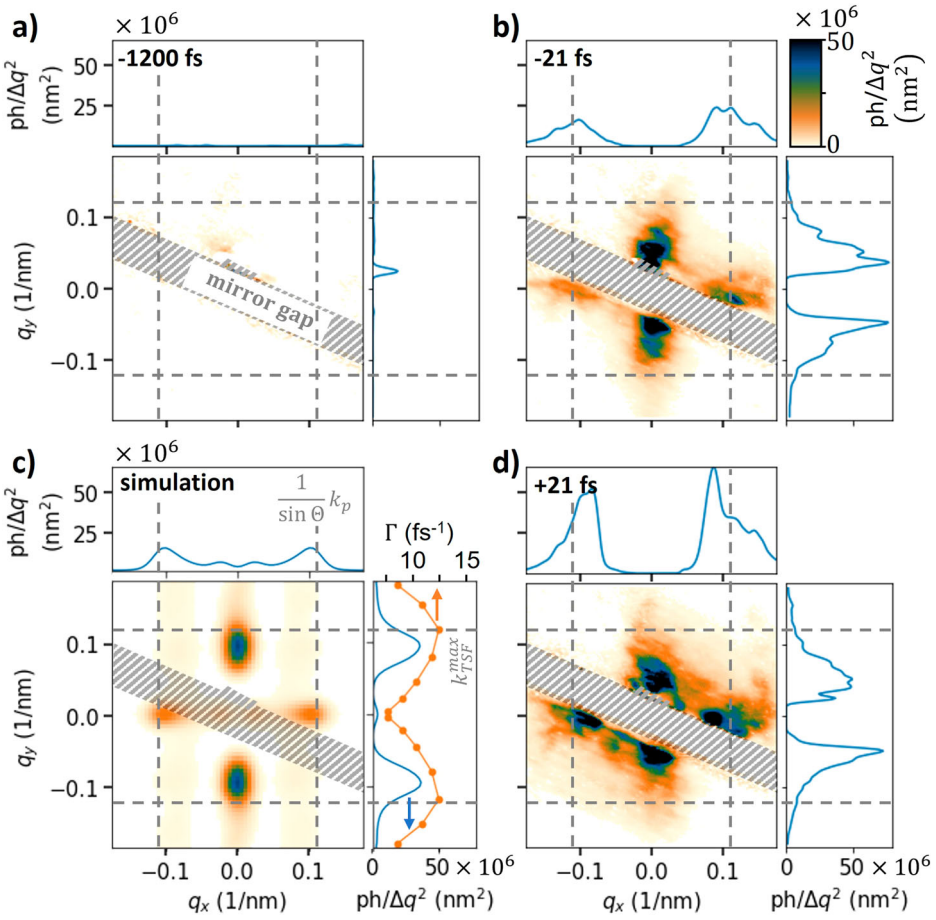

Fig. 2 | Experimental and synthetic scattering patterns. Panels **a**, **b**, and **d** show the background subtracted (as determined by an XFEL-only pre-shot train) and de-noised (using a neural-network (NN) based algorithm) scattering patterns, as photon number per solid angle, recorded by the SAXS detector for three exemplary runs (corrected for HAPG mirror reflectivity and geometry, see methods), the respective probe time delay is indicated in the top panels. The absolute zero delay was defined as the mean value between the two highest signal shots, but was not measured, the relative timing error is below 15 fs (see "Methods" section). The colorbar applies to all panels. The lineouts were taken through $\mathbf{q} = 0$, averaged over ± 0.01 nm^{-1} around $q = 0$. A simulated scattering pattern is shown in **c**) for $t = 0$. The orange line shows the growth rate of the two-stream filamentation (TSF) instability as a function of q_y obtained by numerically solving the dispersion relation. The dashed lines show the analytic theoretical expectation (for the TSF in y-direction, and the bulk plasmons in x-direction, Eq. (2)).

patterns show the dominant signal around the ReLaX laser peak arrival time along the vertical direction (momentum transfer along the laser magnetic field direction) and horizontal direction (momentum transfer in the plane of the laser axis, the laser electric field vector, and the target normal).

In Fig. 3, we show the integrated number of photons recorded along the horizontal and vertical direction for all the 6 data shots that we took for this study. Note that up to -1 ps no significant scattering was measurable, as expected from a flat membrane. At $t = -(31 \pm 13)$ fs the signals are still consistent with zero signal within a 2σ confidence interval. A large scattering signal then sharply occurs at $-(21 \pm 13)$ fs, remaining high for approximately the laser pulse duration. This is an ultra-fast temporal growth of more than two orders of magnitude within 10–30 fs, which shows that the measurements have indeed happened during or shortly after the UHI laser irradiation.

These scattering signals are indicative for a growth of correlated plasma electron density modulations on the timescale of only a few femtoseconds.

Simulations described in the next section (Fig. 4) confirm these findings. To identify the dominant instability mode, we solve the dispersion relation numerically. For our case we find the fastest growing mode is the oblique/two-stream filamentation instability (TSFI) in the front of the foil. The filamentation part is responsible for the signal in vertical direction, while the horizontal signal is originating from scattering on plasmons excited by the laser accelerated electrons traversing the bulk and being subjected to the two-stream instability. A synthetic, forward-calculated scattering image showing the two scattering features from our simulations is shown in Fig. 2c.

Discussion

A cross-like pattern in Fourier space corresponds to a mesh-like pattern in real space. This means that the experimental data directly confirms without any further assumptions that the flat membrane must have developed a corresponding mesh-like electron density pattern in the electron density projected along the XFEL direction according to Eq. (1) as has long been expected from simulations[52,65]. Resulting in a direct measurement of plasma instabilities and plasmons in high-intensity laser-driven solids during or shortly after the irradiation on a few nanometer spatial scale.

To answer the question of the origin of the scattering pattern, we turn to possible instabilities that are known to generate a grating-like pattern. These include, for example, RTI, WI, or CFI, but we could also consider a combination of different waves and instabilities for the different orientations. The situation is further complicated by the high sensitivity of growth rates e.g. to collisions[51] and the momentum distribution of the beam and bulk electrons[52]. In fact, since there exists no previous direct measurement of the solid density plasma break up during the ultra-short laser pulse irradiation in literature, we have to resort to simulations of the UHI laser interaction with the silicon membrane in order to identify and describe quantitatively the plasma dynamics at play.

In Fig. 4, we summarize the results of our simulation, which suggests that the scattering signal that corresponds to a mesh-like projected density profile is, in fact, generated by two rather independent structures that each generate a comb-like density, rotated 90° w.r.t each other.

First, we find a rapidly growing instability mode in the vertical direction (i.e. a density comb in the y-direction with horizontal lines along the x-direction). The density modulations extend inside the target from the front surface with a filament distance of ~63 nm (i.e. $k_y^{\mathrm{PIC}} \sim 0.1\,\mathrm{nm}^{-1}$) and are witnessed by corresponding magnetic field filaments. The density modulation strength grows within several femtoseconds during and shortly after the laser irradiation (growth rate $\Gamma_y^{\mathrm{sim}} \cong 0.1\,\mathrm{fs}^{-1}$) and is static, i.e. not moving over time, see Fig. 4b. The lower bound for the growth rate extracted from the experiment, which is a convolution of the instability modulation strength and the spatial extend of the filaments (dashed line Fig. 3, 1σ confidence interval) is with $0.09\,\mathrm{fs}^{-1}$ in reasonable agreement with the simulation. Also, the spatial scale corresponding to the experimentally

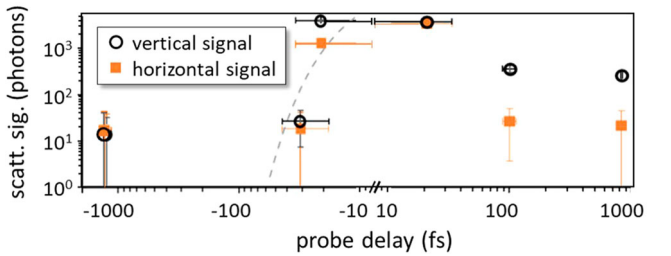

Fig. 3 | Integrated background subtracted scattering signal strength as a function of probe delay. The projected signal around the peaks was integrated over the scattering signal above the noise level in the respective direction. The probe delay was extracted from the pulse arrival monitor. The vertical error bars indicate the background subtraction uncertainty and Poisson counting statistics. The horizontal error bars show timing uncertainty. The relative timing uncertainty is below 15 fs for all shots (absolute timing as in Fig. 2).

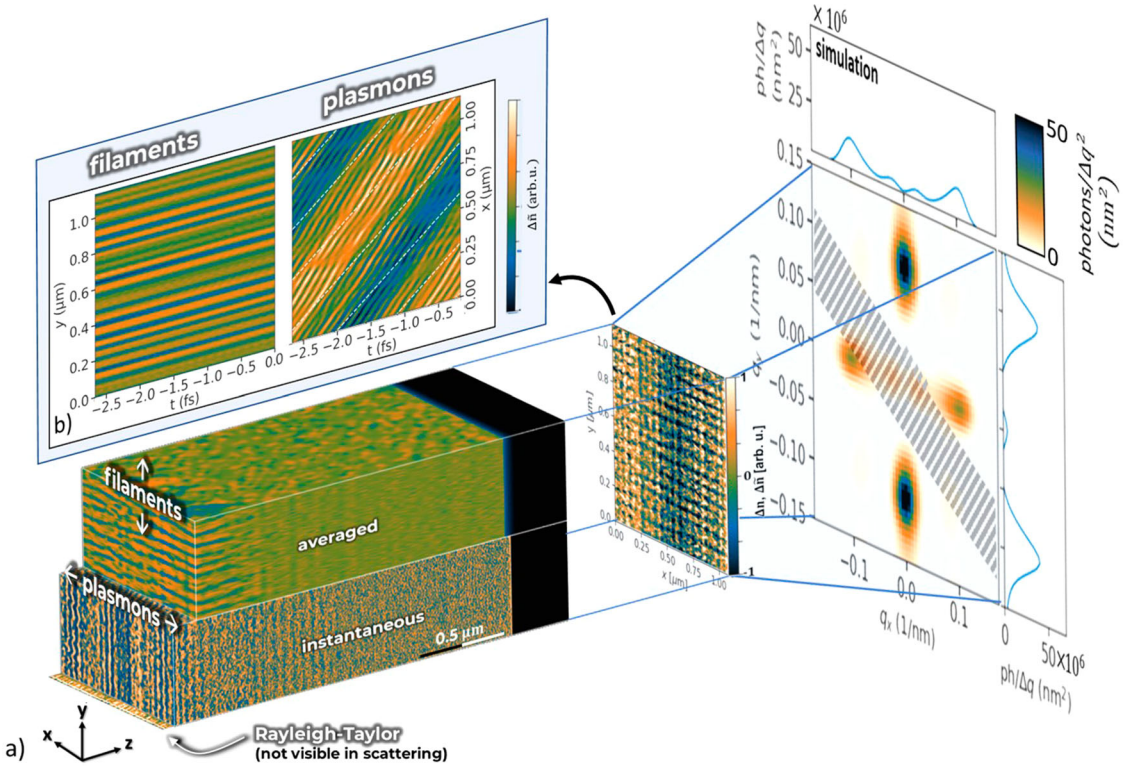

Fig. 4 | Simulation. a Left: Instantaneous and averaged (over a plasma wavelength of 40 nm) electron density deviation from the average target density close to $t = 0$. The superposition of both creates the mesh-like pattern seen in $\tilde{n}_e$ (center). The mesh generates a cross-like pattern in the synthetic scattering signal $\propto \mathfrak{F}(\tilde{n}_e)$ (right). **b** Time evolution of $\tilde{n}_e$ averaged along x (left) and y (right) show that the filamentation pattern is static while the plasmon features are moving with close to $\sqrt{2}c$.

observed scattering wave vector is in reasonable agreement, though somewhat larger than in the simulation.

The simulation suggests that the vertical instability is due to the inhomogeneous current distribution, since it is spatially aligned along the laser-generated electron current. To identify the exact instability mode one has to compute the dielectric tensor and find the solution to the dispersion relation that maximizes the imaginary part of the wave frequency. Because analytic theories rely on specific idealized electron distribution functions, we cannot directly use them here. For example, it is not obvious how to define the fast forward and the fast and bulk return currents, as they continuously merge into another[66]. Rather, we extract the full electron distribution function from the simulation and solve both the integrals in the dielectric tensor and the dispersion relation numerically (i.e. Eq. 6, and Eqs. 16 and 17 in ref. 18 for the Weibel and two-stream filamentation (TSF) branch of the dispersion relation, respectively), assuming the ions are at rest and neglecting magnetic fields. As one might expect from the analytic treatment in the idealized two-stream case, the pure filamentation and Weibel-like modes on the TSF-branch are lost due to the effects of transverse beam and plasma temperature (or more generally: broad energy distribution), respectively. Instable areas are recovered both on the Weibel branch as well as oblique modes on the TSF branch. Yet, in our case the growth rates observed in the latter largely dominate over the former, so that the system is dominated by the oblique modes, also called electromagnetic beam-plasma instability[67] or two-stream filamentation instability[18]. While for the cold case the maximum growth rate of the TSFI is found at $k^{\max} = \infty$, temperature effects stabilize small wavelengths by preventing pinching to small radii[68]. Numerically solving the dispersion relation we find the growth rate is maximized at $k_y^{\max} = 0.12\,\mathrm{nm}^{-1}$ with $\Gamma^{\max} = 12\,\mathrm{fs}^{-1}$ (orange line in Fig. 3). While this value of $k_y^{\max}$ is close to k_y^{PIC} in the simulation, the growth rate is much larger than Γ_y^{sim}. This would mean that the instability is in continuous saturation and in the simulation we rather measure the growth of the saturation limit.

In the horizontal direction (in the laser polarization plane) we do not observe unstable modes due to the stabilizing effect of a larger electron momentum spread, i.e. effective temperature. This is due to the action of the laser electric field, which accelerates each of the 2ω electron bunches, generated by the $\mathbf{v} \times \mathbf{B}$ force, in alternately slightly different directions.

Instead, the integrated density $\tilde{n}_e$ from the simulation shows a dynamic electron plasma wave structure moving with superluminal phase velocity $v_{p,x} = c/\sin\Theta$ transverse to the XFEL, where $\Theta = \pi/4$ is the laser incidence angle w.r.t. the target normal. Along the laser direction electrons are accelerated to close the speed of light, which excite bulk plasma oscillations as they propagate through the plasma (i.e. the two-stream instability part of the TSFI) with a phase velocity also close to the speed of light. The XFEL phase fronts cut through this plasmon structure under the angle Θ; the superluminosity of the apparent phase velocity $v_{p,x}$ is, therefore, merely a geometric effect in the projection on the XFEL probe plane. The plasma oscillations appear as a traveling periodic wave-like density comb with vertical lines in the density projection along the XFEL direction with the projected wave vector

$$k_{p,x} = \frac{\omega_{pe}}{v_{p,x}} \approx 0.11\,\mathrm{nm}^{-1} \tag{2}$$

corresponding to $\lambda_{p,x} = 56$ nm ($\omega_{pe} \cong 47\,\mathrm{fs}^{-1}$ is the plasma frequency), see right panel in Fig. 4b.

It is important to point out that this dynamic feature can only be measured by means of scattering, since in shadowgraphic probing the projection of the time-integrated density is measured, which would almost completely smear out for the traveling plasmons and probes longer than the plasmon period.

After the laser pulse maximum on target, the horizontal plasmon signal vanishes almost immediately, i.e., at 100 fs, it drops to the noise level. This is intuitively clear since it is bound to the plasma oscillations excited in the wake of the laser accelerated electron beam. In the vertical direction the filamentation signal also decreases but stays above the noise level throughout the observation time window of 1 ps. This could be due to the expected merging of the filaments and hence a shift of the signal towards a q value below our detection threshold, as also observed in the simulation (Supplementary Figs. 5 and 6).

A synthetic scattering pattern computed from the simulation over two laser periods around the peak intensity arrival on target is shown in Fig. 2 and allows a direct comparison with the experiment. The general structures are in good agreement with the experiment, both quantitatively and qualitatively. In the horizontal direction, the scattering peaks are nearly at the same position in simulation and experiment, while there is a slight mismatch in the vertical direction. Indirect measurements always had the problem that such small deviations could in principle be attributed to the complex processes involved in the measurement, in contrast here we have a clear indication for a different TSFI wavelength measured than observed in the simulation which is indicative for differences in the electron momentum distribution, i.e. the laser generated electron current and return current (e.g. beam energy, temperature, density).

Another important aspect is the intensity ratio between the vertical and horizontal signals. While the filaments exist over the full laser pulse duration and beyond while merging relatively slowly, due to the comparatively slow magnetic diffusion time scales, the plasmonic signal essentially stops when the laser pulse is over. Hence, at later times we expect the vertical signal to be much larger than the horizontal one (within the laser polarization plane), by up to two orders of magnitude at 30 fs after the laser peak based on our simulation. The fact that we experimentally observe this strong difference between the vertical and horizontal signal strengths indeed only at the larger delays $t \geq 100$ fs is therefore an additional indication for having probed the plasma around the laser peak.

Of course, other instabilities can in principle not be ruled out as a source for the experimentally observed correlations, since the simulations and model are subject to simplifications. For example, in our simulations a Rayleigh-Taylor-like instability develops at the front surface, which we rule out as the source of the measured signal due to its much smaller wave-vector than detectable with the current setup, and its much smaller predicted scattering signal than that of the filaments.

Conclusions

Combining the experiments, simulations and analytic estimates, we can draw a complete picture of the most likely plasma dynamics in the current experiment: As the relativistic laser accelerated forward electron current streams through the bulk return current transverse filaments are growing rapidly during the laser irradiation, and at the same time longitudinal plasmons are driven. Both filaments and plasmons add up to generate a mesh-like electron density pattern that is responsible for the measured cross-like scattering pattern. This is the first ultra-fast dynamic signal visualized from UHI laser-driven solids on the few nanometer scale, highlighting the great potential of SAXS for studying the early time of UHI-solid interaction dynamics. We measured the spatial electron density correlations to few-nanometer, few-femtosecond precision, which is in reasonable qualitative agreement with our simulations that favor the TSFI. More comprehensive measurements of the growth rates and spatial scales will allow to refine and benchmark our simulations and overall knowledge of important key topics in relativistic plasma physics, including laser absorption, return current generation, instability growth and thermal stabilization, via the dispersion relation. For example, the growth rate dependency on the electron beam Lorentz factor γ is distinctly different between WI ($\propto \gamma^{-1}$), CFI ($\propto \gamma^{-1/2}$), and TSFI ($\propto \gamma^{-1/3}$), and the instability spectrum in k-space depends on the electron momentum distribution via the dielectric tensor.

Methods

Experimental procedure

ReLaX and XFEL properties. The Titanium:Sapphire high-intensity short-pulse laser ReLaX has a wavelength of $\lambda_L = 0.8\,\mu$m. The measured focus size of the ReLaX laser was approx. $w_L = 4.7\,\mu$m FWHM. The laser

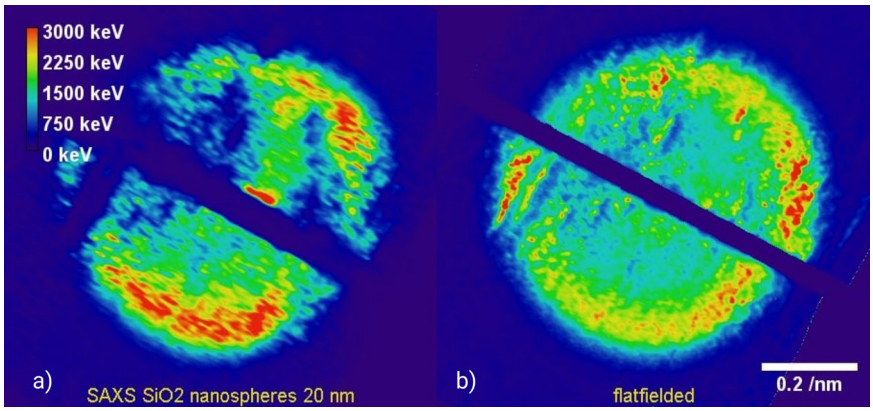

Fig. 5 | Flatfield. Small-angle X-ray scattering (SAXS) signal from SiO2 nanospheres (20 nm diameter before **a**) and after correction (**b**) as described in ref. 64.

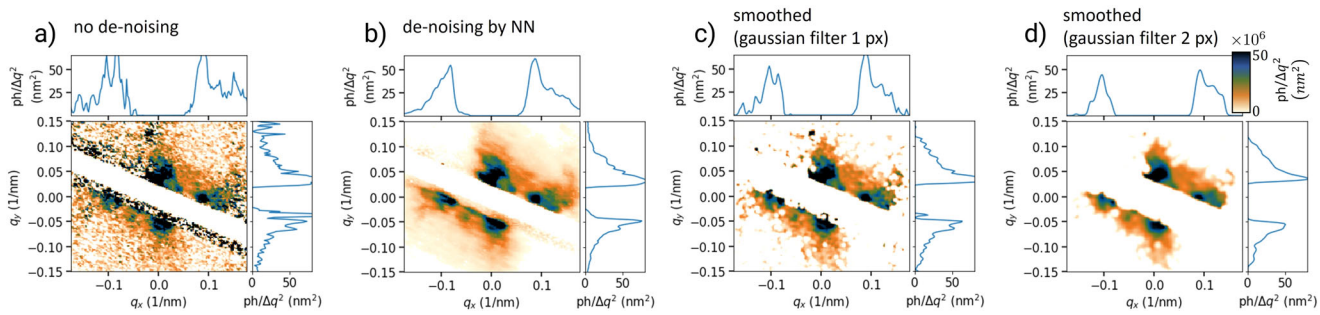

Fig. 6 | Denoising. Example for denoising of the data, exemplified on the data shown in Fig. 2 (21 fs delay). **a**: no denoising applied, only flat-fielding correction was used. **b** de-noising by the Neural Network (NN) was applied. **c**, **d**: Same as left, but log-smoothed (i.e. the log of the data was smoothed) with a gaussian filter of width 0.002 nm^{-1} (i.e. 1 px) and 0.004 nm^{-1} (i.e. 2 px). The colorbar in **d** applies to all panels. Note how the fine structure is preserved for de-noising using the NN compared to smoothing.

pulse energy, duration and calculated intensity were $W_L \approx 2.8$ J, $\tau_L = 30$ fs, and 5×10^{20} W cm^{-2} ($a_0 = 15$), respectively.

The XFEL beam was used in the self-amplified spontaneous emission (SASE) configuration with a wavelength of $\lambda_X = 0.15$ nm (=8 keV). The focal spot was $w_X \approx 20\,\mu$m FWHM, the XFEL energy, duration, and calculated number of photons were $W_X \approx 1.5$ mJ, $\tau_X \approx 30$ fs, and $N_X \approx 1.2 \times 10^{12}$ photons per bunch. The XFEL fundamental was dumped on an X-ray detector 4 m downstream of the target.

Synchronization. The XFEL probe time delay given in the figures is the relative timing measured with the HED (High Energy Density Science) optical encoding pulse arrival monitor (PAM) to a precision of 12.9 fs w.r.t. the nominal zero delay set for all runs[60]. The nominal zero delay was not calibrated for the shots in this work, so that this is largely unknown due to drift and the jitter. We therefore give all times relative to the central time between the two highest yield shots.

SAXS signal processing. THE SAXS signal is reflected by the HAPG mirror to the Jungfrau detector. The reflectivity of the mirror is approx. 0.2. As the reflectivity of the mirror is varying over its surface, it has to be corrected by a flat-field inferred from the scattering on a known substance, we employed SiO2 nanospheres target with particle diameter 20 nm, as described in ref. 64. The geometrical distortion of the signal was also corrected by a scheme described there, see Fig. 5. Then, the data was de-noised (cp. Fig. 6) using a custom-made neural network trained on the experimental background added to synthetic data[69]. On this corrected data, the signal from XFEL-only pre-shot (Fig. 7) was subtracted (normalized to the main shot by gas detector measurements for the XFEL intensity), as this resembles the parasitical scattering not originating in the target.

Quantitative analysis of scattering signal. In Fig. 3 the vertical/horizontal signals were projected along the perpendicular direction over a band 25 px wide around the peaks. Along the vertical/horizontal direction the signal was then integrated around peaks in the region where this projected signal was 2σ above the background. The error bars in the figure indicate the background subtraction uncertainty and Poisson counting statistics. The uncertainty due to the XFEL spatial jitter is not included.

Simulations and modeling

Simulation setup. 3D Simulations were performed using PIConGPU[70,71] with spatial resolution $\Delta x = \Delta y = \Delta z \approx 2\pi c \omega_{pe}^{-1}/17$, where $\omega_{pe} = 20\omega_L$, and 8 macro ions per cell. The silicon foil was preionized to the +3 state with one macro electron per macro ion (These electrons have an initial temperature $T_e = 0.1$ keV). Ionization was included via barrier suppression, Ammosov-Delone-Krainov (ADK) and a modified Thomas-Fermi models to correct for low temperatures, low densities as described in the PIConGPU documentation. A 50 nm exponential preplasma was added to the front target surface to account for amplified spontaneous emission (ASE) and the laser pedestal finite contrast. Additionally, we performed a set of 2D simulations that confirmed that the qualitative results do not sensitively depend on the preplasma in the few 10s of nm scale range. We observed filament formation in all simulations with the dominant spatial frequency always between 50 and 90 nm, see the 2D Simulations: preplasma scale length scan section of the Supplementary Methods, and Supplementary Figs. 2,3,4. The same is true for hole boring by the spatial intensity profile of the UHI laser: Previous simulations have shown no qualitative change of the dynamics in the small volume around the laser axis between simulations with and without taking into account the pulse

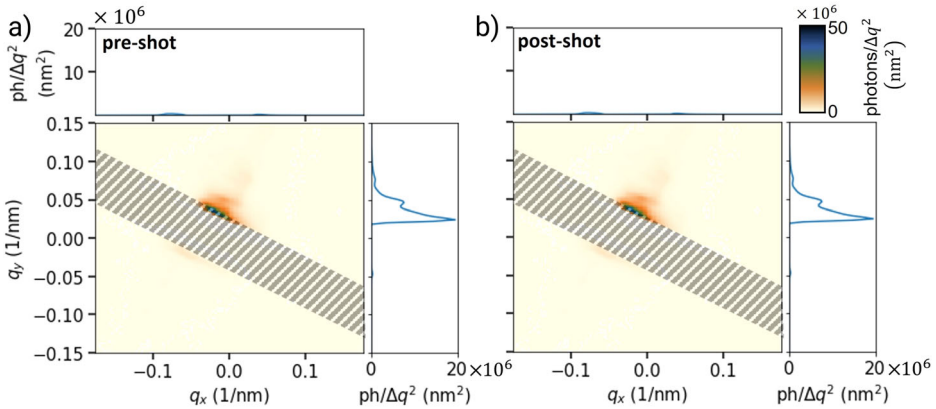

Fig. 7 | Pre-shot and Post-shot. XFEL-only pre-shot (**a**) and post-shot (**b**) show exemplarily for the shot of delay −20 fs the parasitic signal that was subtracted from the main-shots in Fig. 2. The colorbar in **b** applies to both panels.

shape[65]. The simulated laser is a 30 fs Gaussian p-polarized plane wave with $a_0 = 15$ peak normalized amplitude propagating at a 45° to the target normal and is initialized 2.5 · FWHM before and after the max intensity. The transversal box size $L_{\mathrm{sim,x}} = L_{\mathrm{sim,y}} = \sqrt{(2)}\,\lambda_{\mathrm{L}}$ was chosen to match the laser phase at the periodic boundaries (in the transversal direction), $L_{\mathrm{sim},z} = 5.08\,\lambda_{\mathrm{L}}$. With $L_{\mathrm{sim},x}/(\sqrt{2}c)$ being much smaller than the timescale at which the laser envelope changes, we can approximate the laser amplitude to be the same on both sides of the transversal boundary in x. Satisfying those two conditions allows us to combine the 45° laser incidence with the transversal periodic boundaries. The 2 μm thick (excluding preplasma) planar target was placed (its front surface) at $z = 1$ μm. The field propagation is done with the standard Yee field solver and the absorption at the boundaries in the longitudinal direction is realized with a perfectly matched layer (PML). For particles, we use a 4th order shape together with the Higuera-Cary pusher.

To prove that the simplifying assumptions of the limited size 3D simulations are indeed not causing problems such as Moire interference of filaments induced by the periodic boundaries, or discrepancies in the dynamics caused by the transversely plane laser ignoring the finite spot size, we show in the Supplementary Methods section IA (2D Simulations: preplasma scale length scan) and in the Supplementary Fig. 1 a 2D simulation with similar numerical parameters as the 3D simulation in the main text.

Synthetic SAXS pattern. The synthetic SAXS pattern I^{synth} was computed by first computing $\tilde{n}_{\mathrm{e}}$[72], and taking its Fourier transform absolute square. The resulting signal was averaged over a time of 3 fs. Note that the real XFEL pulse duration was longer, the time here was reduced due to large storage requirement of the 3D data set. To get a quantitative estimate of the expected photons on the detector, I^{synth}, the simulated X-ray signal was then scaled to the experimental intensity assuming scattering only within the ReLaX focus (FWHM) with the time average of the simulated intensity. That means, I^{synth} was normalized such that $I^{\mathrm{synth}}(\mathbf{Q} = \mathbf{0}) = r_{\mathrm{e}}^2 N_{\mathrm{X}} (w_{\mathrm{L}}/w_{\mathrm{X}})^2 / w_{\mathrm{L}}^2 \cdot N_{\mathrm{e}}^2 \Delta\Omega$ (see Eq. (6) in ref. 43), where $N_{\mathrm{e}} = 410 \cdot n_{\mathrm{c}} w_{\mathrm{L}}^2 \cdot 2\,\mu$m is the estimate number of electrons within the ReLaX focus where $n_{\mathrm{c}} = 2\pi m_{\mathrm{e}} \lambda_{\mathrm{L}} \varepsilon_0 / (ce^2)$ is the critical density (with m_{e}, e the electron mass and charge, and ε_0 the vacuum permeability), w_{L}^2 the probed area, $\Delta\Omega$ is the solid angle corresponding to $(\Delta q)^2 = \mathrm{nm}^{-2}$, and r_{e} is the classical electron radius. Note: The similarity of the projected plasma wavelength, $\lambda_x^{\mathrm{PIC}} \cong 2\pi c/(\omega_{\mathrm{pe}} \sin(\pi/4)) = 60$ nm, with the vertical filamentation wavelength $\lambda_y^{\mathrm{PIC}} = 70$ nm most likely is coincidence, as we repeated the simulation with a more shallow laser incidence angle of 22.5°. There, λ_x is reduced as expected, while λ_y remains constant.

Growth rate and filamentation wave vector. The instability spectrum of the fastest mode plotted in Fig. 2 (orange dashed line) was obtained from the PIC simulation at $t = 0$. We first binned the electron momenta from the region with visible filaments 1.3 μm > z < 2.0 μm, see Supplementary Fig. 5, into bins of size $\Delta(\gamma\beta) = 0.05$. We then checked for roots of the dispersion relation Eq. (15) in ref. 18, with x into laser direction and z into the filamentation direction. Eq. (6) in that paper was solved numerically using the Landau contour: First, we rotated the coordinate system such that the root lies along a coordinate axis $\mathbf{e}_\alpha$. Then, for each p_α we computed and summed up the residue and integral along p_β, with symmetric bins around the root of the denominator of the second integral, again with a resolution of $\Delta(\gamma\beta) = 0.05$, and with the derivation of $f(\mathbf{p})$ at $\mathbf{p}_0$ taken symmetric around $\mathbf{p}_0$.

This approach assumes a homogeneous plasma, which we ensure imposes periodic boundary conditions and a transversely plane laser. This is justified in the laser focus, where the laser intensity changes only slowly over the micron scale and which is large compared to the filamentation scale of tens of nanometers. However, as boundary effects are neglected, the model does not account for the change in density at the target front and back surfaces; hence, surface instabilities such as, e.g., the RTI, are not included. Also, the theory is only applicable in the linear phase of instability growth.

Why do the plasmons not smear out the signal in SAXS? While in shadowgraphic methods, the XFEL-propagation at a large angle w.r.t. orientation of the plasmon propagation leads to their contrast almost vanishing for probes longer than the projected plasmon period due to smearing out the density contrast, for X-ray scattering the signal of a pattern $\tilde{n}(\mathbf{r})$ moving with velocity $v_{\mathrm{p},x}$ in x-direction is approximately given by the integral over the XFEL irradiated area and XFEL pulse duration

$$I(\mathbf{q}) \propto \int_t \left| \int_w \tilde{n}(\mathbf{r}) \mathrm{e}^{\mathrm{i}(q_x v_{\mathrm{p}})t} \mathrm{e}^{-\mathrm{i}\mathbf{q}\mathbf{r}} \mathrm{d}\mathbf{r} \right|^2 \mathrm{d}t \propto |FT(\tilde{n}(\mathbf{r}))|^2,$$

i.e. simply the usual Fourier transform absolute square of the static density pattern.

Data availability

Data recorded for the experiment at the European XFEL are available at XFEL[73]. The processed data and simulation data, as well as the scripts used to generate Figs. 2–4 are available at Rodare data repository[74].

Code availability

The custom code used for the numerical solving of the dispersion relation is available from the authors upon reasonable request. The code used to generate synthetic scattering patterns from simulation output was published on Zenodo[72]. The denoising code[69] is currently under embargo and will be

published in a separate paper, the authors are available to collaborate upon reasonable request.

Received: 26 January 2024; Accepted: 12 August 2024;
Published online: 03 September 2024

References

1. Kroll, F. et al. Tumour irradiation in mice with a laser-accelerated proton beam. *Nat. Phys.* **18**, 316–322 (2022).
2. Albert, F. et al. 2020 roadmap on plasma accelerators. *N. J. Phys.* **23**, 031101 (2021).
3. Craxton, R. S. et al. Direct-drive inertial confinement fusion: a review. *Phys. Plasmas* **22**, 110501 (2015).
4. Edwards, C. & Danson, C. Inertial confinement fusion and prospects for power production. *High. Power Laser Sci. Eng.* **3**, e4 (2015).
5. Zylstra, A. et al. *IFE Science & Technology Community Strategic Planning Workshop Repory* https://lasers.llnl.gov/sites/lasers/files/2022-11/IFE-Workshop-Report.pdf (2022).
6. Wilks, S. C. et al. *Short Pulse Laser based Ion Fast Ignition for IFE*. Whitepaper for LLNL-IFE-workshop LLNL-CONF-831230. https://lasers.llnl.gov/sites/lasers/files/2023-11/wilks-LLNL-IFE-workshop-2022.pdf (2022).
7. Obst-Huebl, L. et al. *BELLA PW 1 Hz Laser Experiments for Short Pulse Laser-based Ion Fast Ignition for IFE* https://lasers.llnl.gov/sites/lasers/files/2023-11/obsthuebl-LBNL-IFE-workshop-2022.pdf (2022).
8. Abu-Shawareb, H. et al. Lawson criterion for ignition exceeded in an inertial fusion experiment. *Phys. Rev. Lett.* **129**, 075001 (2022).
9. Bishop, B. *National Ignition Facility Achieves Fusion Ignition*. LLNL press release https://www.llnl.gov/news/national-ignition-facility-achieves-fusion-ignition (2022).
10. Glenzer, S. H. et al. Symmetric inertial confinement fusion implosions at ultra-high laser energies. *Science* **327**, 1228–1231 (2010).
11. Remington, B. A. et al. Rayleigh–Taylor instabilities in high-energy density settings on the National Ignition Facility. *Proc. Natl Acad. Sci. USA* **116**, 18233–18238 (2019).
12. Mahdavi, M. & Khanzadeh, H. The effect of the plasma density gradient on current filamentation instability. *Contrib. Plasma Phys.* **61**, e202100027 (2021).
13. Badziak, J. & Domański, J. In search of ways to improve the properties of a laser-accelerated heavy ion beam relevant for fusion fast ignition. *Phys. Plasmas* https://pubs.aip.org/pop/article/30/5/053107/2890110/In-search-of-ways-to-improve-the-properties-of-a (2023).
14. Tabak, M. et al. Ignition and high gain with ultrapowerful lasers. *Phys. Plasmas* **1**, 1626–1634 (1994).
15. Roth, M. et al. Fast ignition by intense laser-accelerated proton beams. *Phys. Rev. Lett.* **86**, 436–439 (2001).
16. Campbell, E. M. et al. Direct-drive laser fusion: status, plans and future. *Philos. Trans. R. Soc. A* **379**, 20200011 (2021).
17. Macchi, A. et al. Fundamental issues in fast ignition physics: from relativistic electron generation to proton driven ignition. *Nucl. Fusion* **43**, 362 (2003).
18. Bret, A., Firpo, M. C. & Deutsch, C. Collective electromagnetic modes for beam-plasma interaction in the whole k space. *Phys. Rev. E - Stat. Phys. Plasmas Fluids Relat. Interdiscip. Top.* **70**, 15 (2004).
19. Metzkes, J. et al. Experimental observation of transverse modulations in laser-driven proton beams. *N. J. Phys.* **16**, 23008 (2014).
20. Göde, S. et al. Relativistic electron streaming instabilities modulate proton beams accelerated in laser-plasma interactions. *Phys. Rev. Lett.* **118**, 194801 (2017).
21. Scott, G. G. et al. Diagnosis of Weibel instability evolution in the rear surface density scale lengths of laser solid interactions via proton acceleration. *N. J. Phys.* **19**, 043010 (2017).
22. Huang, L. G., Schlenvoigt, H. P., Takabe, H. & Cowan, T. E. Ionization and reflux dependence of magnetic instability generation and probing inside laser-irradiated solid thin foils. *Phys. Plasmas* **24**, 103115 (2017).
23. Macchi, A., Cornolti, F. & Pegoraro, F. Two-surface wave decay. *Phys. Plasmas* **9**, 1704–1711 (2002).
24. Palmer, C. A. et al. Rayleigh-Taylor instability of an ultrathin foil accelerated by the radiation pressure of an intense laser. *Phys. Rev. Lett.* **108**, 225002 (2012).
25. Khudik, V., Yi, S. A., Siemon, C. & Shvets, G. The analytic model of a laser-accelerated plasma target and its stability. *Phys. Plasmas* **21**, 013110 (2014).
26. Kluge, T. et al. Two surface plasmon decay of plasma oscillations. *Phys. Plasmas* **22**, 64502 (2015).
27. Sgattoni, A., Sinigardi, S., Fedeli, L., Pegoraro, F. & Macchi, A. Laser-driven Rayleigh-Taylor instability: plasmonic effects and three-dimensional structures. *Phys. Rev. E - Stat., Nonlinear Soft Matter Phys.* **91**, 013106 (2015).
28. Eliasson, B. Instability of a thin conducting foil accelerated by a finite wavelength intense laser. *N. J. Phys.* **17**, 033026 (2015).
29. Chou, H.-G. J., Grassi, A., Glenzer, S. H. & Fiuza, F. Radiation pressure acceleration of high-quality ion beams using ultrashort laser pulses. *Phys. Rev. Res.* **4**, L022056 (2022).
30. Macchi, A. et al. Surface oscillations in overdense plasmas irradiated by ultrashort laser pulses. *Phys. Rev. Lett.* **87**, 205004–1 (2001).
31. Sentoku, Y., Mima, K., Kojima, S. I. & Ruhl, H. Magnetic instability by the relativistic laser pulses in overdense plasmas. *Phys. Plasmas* **7**, 689–695 (2000).
32. Sentoku, Y. et al. Three-dimensional particle-in-cell simulations of energetic electron generation and transport with relativistic laser pulses in overdense plasmas. *Phys. Rev. E - Stat. Phys. Plasmas Fluids Relat. Interdiscip. Top.* **65**, 7 (2002).
33. Sentoku, Y., Mima, K., Kaw, P. & Nishikawa, K. Anomalous resistivity resulting from MeV-electron transport in overdense plasma. *Phys. Rev. Lett.* **90**, 4 (2003).
34. Sokolowski-Tinten, K. et al. Transient states of matter during short pulse laser ablation. *Phys. Rev. Lett.* **81**, 224 (1998).
35. Geindre, J. P. et al. Frequency-domain interferometer for measuring the phase and amplitude of a femtosecond pulse probing a laser-produced plasma. *Opt. Lett.* **19**, 1997 (1994).
36. Bocoum, M. et al. Spatial-domain interferometer for measuring plasma mirror expansion. *Opt. Lett.* **40**, 3009 (2015).
37. Malvache, A., Borot, A., Quéré, F. & Lopez-Martens, R. Coherent wake emission spectroscopy as a probe of steep plasma density profiles. *Phys. Rev. E - Stat. Nonlinear Soft Matter Phys.* **87**, 035101 (2013).
38. Zhou, S. et al. Self-organized kilotesla magnetic-tube array in an expanding spherical plasma irradiated by kHz femtosecond laser pulses. *Phys. Rev. Lett.* **121**, 255002 (2018).
39. Quinn, K. et al. Weibel-induced filamentation during an ultrafast laser-driven plasma expansion. *Phys. Rev. Lett.* **108**, 135001 (2012).
40. Raj, G. et al. Probing ultrafast magnetic-field generation by current filamentation instability in femtosecond relativistic laser-matter interactions. *Phys. Rev. Res.* **2**, 023123 (2020).
41. Fletcher, L. B. et al. Ultrabright X-ray laser scattering for dynamic warm dense matter physics. *Nat. Photon.* **9**, 274–279 (2015).
42. Gorkhover, T. et al. Femtosecond and nanometre visualization of structural dynamics in superheated nanoparticles. *Nat. Photon.* **10**, 93–97 (2016).
43. Kluge, T. et al. Nanometer-scale characterization of laser-driven compression, shocks, and phase transitions, by x-ray scattering using free electron lasers. *Phys. Plasmas* **24**, 102709 (2017).
44. Kluge, T. et al. Observation of ultrafast solid-density plasma dynamics using femtosecond X-ray pulses from a free-electron laser. *Phys. Rev. X* **8**, 031068 (2018).

45. Mo, M. et al. Visualization of ultrafast melting initiated from radiation-driven defects in solids. *Sci. Adv.* **5**, eaaw0392 (2019).
46. Gaus, L. et al. Probing ultrafast laser plasma processes inside solids with resonant small-angle x-ray scattering. *Phys. Rev. Res.* **3**, 043194 (2021).
47. Davidson, R. C. Nonlinear development of electromagnetic instabilities in anisotropic plasmas. *Phys. Fluids* **15**, 317 (1972).
48. Tatarakis, M. et al. Propagation instabilities of high-intensity laser-produced electron beams. *Phys. Rev. Lett.* **90**, 4 (2003).
49. Bret, A., Firpo, M.-C. & Deutsch, C. Characterization of the initial filamentation of a relativistic electron beam passing through a plasma. *Phys. Rev. Lett.* **94**, 115002 (2005).
50. Bret, A., Firpo, M.-C. & Deutsch, C. Electromagnetic instabilities for relativistic beam-plasma interaction in whole k space: nonrelativistic beam and plasma temperature effects. *Phys. Rev. E* **72**, 016403 (2005).
51. Cottrill, L. A. et al. Kinetic and collisional effects on the linear evolution of fast ignition relevant beam instabilities. *Phys. Plasmas* https://pubs.aip.org/pop/article/15/8/082108/897086/Kinetic-and-collisional-effects-on-the-linear (2008).
52. Bret, A., Gremillet, L. & Bénisti, D. Exact relativistic kinetic theory of the full unstable spectrum of an electron-beam–plasma system with Maxwell-Jüttner distribution functions. *Phys. Rev. E* **81**, 036402 (2010).
53. Bret, A., Stockem, A., Narayan, R. & Silva, L. O. Collisionless Weibel shocks: full formation mechanism and timing. *Phys. Plasmas* **21**, 072301 (2014).
54. Jung, R. et al. Study of electron-beam propagation through preionized dense foam plasmas. *Phys. Rev. Lett.* **94**, 195001 (2005).
55. Allen, B. et al. Experimental study of current filamentation instability. *Phys. Rev. Lett.* **109**, 185007 (2012).
56. Zhang, C. et al. Ultrafast optical field–ionized gases—a laboratory platform for studying kinetic plasma instabilities. *Sci. Adv.* **5**, eaax4545 (2019).
57. Sherlock, M., Hill, E. G., Evans, R. G., Rose, S. J. & Rozmus, W. In-depth plasma-wave heating of dense plasma irradiated by short laser pulses. *Phys. Rev. Lett.* **113**, 255001 (2014).
58. Macchi, A. Surface plasmons in superintense laser-solid interactions. *Phys. Plasmas* https://pubs.aip.org/pop/article/25/3/031906/1060115/Surface-plasmons-in-superintense-laser-solid (2018).
59. Fedeli, L. et al. Electron acceleration by relativistic surface plasmons in laser-grating interaction. *Phys. Rev. Lett.* **116**, 015001 (2016).
60. Laso Garcia, A. et al. ReLaX: the Helmholtz International Beamline for Extreme Fields high-intensity short-pulse laser driver for relativistic laser–matter interaction and strong-field science using the high energy density instrument at the European X-ray free electron laser fa. *High. Power Laser Sci. Eng.* **9**, E59 (2021).
61. HIBEF Consortium. http://www.hibef.eu
62. Nakatsutsumi, M. & Tschentscher, T. Conceptual Design Report: Scientific Instrument High Energy Density Physics (HED). Tech. Rep., *European X-Ray Free-Electron Laser Facility GmbH* https://www.xfel.eu/sites/sites_custom/site_xfel/content/e35165/e46561/e46886/e46963/e46964/xfel_file46965/TR-2013-003_CDR_HED_eng.pdf (2013).
63. Zastrau, U. et al. The high energy density scientific instrument at the european XFEL. *J. Synchrotron. Radiat.* **28**, 1393–1416 (2021).
64. Šmíd, M. et al. Mirror to measure small angle x-ray scattering signal in high energy density experiments. *Rev. Sci. Instrum.* **91**, 123501 (2020).
65. Kluge, T. et al. Using X-ray free-electron lasers for probing of complex interaction dynamics of ultra-intense lasers with solid matter. *Phys. Plasmas* **21**, 033110 (2014).
66. Sherlock, M., Rozmus, W., Hill, E. G. & Rose, S. J. Sherlock et al. Reply. *Phys. Rev. Lett.* **116**, 159502 (2016).
67. Califano, F., Prandi, R., Pegoraro, F. & Bulanov, S. V. Nonlinear filamentation instability driven by an inhomogeneous current in a collisionless plasma. *Phys. Rev. E* **58**, 7837–7845 (1998).
68. Silva, L. O., Fonseca, R. A., Tonge, J. W., Mori, W. B. & Dawson, J. M. On the role of the purely transverse Weibel instability in fast ignitor scenarios. *Phys. Plasmas* **9**, 2458 (2002).
69. Starke, S. & Smid, M. *Software: Removal Of Bremsstrahlung Background From SAXS Signals With Deep Neural Networks* https://doi.org/10.14278/rodare.2586 (2023).
70. Bussmann, M. et al. Radiative signatures of the relativistic kelvin-helmholtz instability. In *Proceedings of the International Conference on High Performance Computing, Networking, Storage and Analysis*, SC '13, 5:1–5:12 (ACM, 2013).
71. Bastrakov, S. et al. *ComputationalRadiationPhysics/picongpu: C++14, New Solvers, I/O via openPMD API, HIP Support* https://doi.org/10.5281/zenodo.5795557(2021).
72. Ordyna, P. *pordyna/saxify: First Release* https://doi.org/10.5281/zenodo.12751592 (2024).
73. Schlenvoigt, H.-P. & Kluge, T. "Kinetic instabilities in the interaction of ultra-intense ultra-short laser pulses with solids". *Experimental data* https://doi.org/10.22003/XFEL.EU-DATA-002854-00 (2022).
74. Kluge, T. & Ordyna, P. *Raw data and data used for figures in "Visualizing Plasmons and Ultrafast Kinetic Instabilities in Laser-Driven Solids using X-ray Scattering"* https://doi.org/10.14278/rodare.2184 (2023).

Acknowledgements

We acknowledge European XFEL in Schenefeld, Germany, for the provision of X-ray free-electron laser beamtime at HED HIBEF (Helmholtz International Beamline for Extreme Fields) SASE2 and would like to thank the staff for their assistance. The authors are indebted to the HIBEF user consortium for the provision of instrumentation and staff that enabled this experiment. Christian Gutt acknowledges funding by DFG (GU 535/6-1). This work has also been supported by HIBEF and partially by the European Commission via H2020 Laserlab Europe V (PRISES) contract no. 871124, and by the German Federal Ministry of Education and Research (BMBF) under contract number 03Z1O511. This research used resources of the National Energy Research Scientific Computing Center (NERSC), a U.S. Department of Energy Office of Science User Facility located at Lawrence Berkeley National Laboratory, operated under Contract No. DE-AC02-05CH11231 using NERSC awards FES-ERCAP0023216 and FES-ERCAP0027292. We would like to express our sincere gratitude to S.V. Rahul from European XFEL for his invaluable insights and fruitful discussions related to this publication.

Author contributions

The experiment was set up and performed by A.L.G and T.T., being responsible for the laser delivery; A.L.G. and M.S. were responsible for the SAXS instrument; M.N. was responsible for timing; U.H., I.P., and H.-P.S. were responsible for the target production and handling; and A.L.G., C.B., E.B., S.G., H.H., O.H., M.N., A.P., T.P., and J.-P.S. as beamline scientists, supported in operation by M.G., L.G., L.H., B.E.M., T.K. Ö.Ö., X.P., F. P.-B., L.R., H.-P. S., M.S, R.S., E.T., K.Z. T.K., and P.O. performed the analysis of the experimental data with support from M.N. (pulse arrival monitor), S.S. (AI background removal), and M.S. (AI background removal, SAXS data processing and interpretation). Numerical simulations were performed by P.O. and interpreted by P.O. and T.K.; P.O. and T.K. wrote the manuscript., T.E.C, U.S., C.G., and T.K. supervised the project. All previously mentioned authors and M.B., J.G., J. M.-N., and T.M. reviewed the manuscript and contributed extensively to discussions.

Funding

Open Access funding enabled and organized by Projekt DEAL.

Competing interests
The authors declare no competing interests.

Additional information
Supplementary information The online version contains supplementary material available at https://doi.org/10.1038/s42005-024-01776-6.

Correspondence and requests for materials should be addressed to Paweł. Ordyna or Thomas Kluge.

Peer review information *Communications Physics* thanks the anonymous reviewers for their contribution to the peer review of this work. A peer review file is available.